Lateral Magnetically Modulated Multilayers by Combining Ion Implantation and Lithography

Enric Menéndez, Hiwa Modarresi, Claire Petermann, Josep Nogués,* Neus Domingo, Haoliang Liu, Brian J. Kirby, Amir Syed Mohd, Zahir Salhi, Earl Babcock, Stefan Mattauch, Chris Van Haesendonck, André Vantomme, and Kristiaan Temst**

The combination of lithography and ion implantation is demonstrated to be a suitable method to prepare lateral multilayers. A laterally, compositionally, and magnetically modulated microscale pattern consisting of alternating Co (1.6 μm wide) and Co-CoO (2.4 μm wide) lines has been obtained by oxygen ion implantation into a lithographically masked Au-sandwiched Co thin film. Magnetoresistance along the lines (i.e., current and applied magnetic field are parallel to the lines) reveals an effective positive giant magnetoresistance (GMR) behavior at room temperature. Conversely, anisotropic magnetoresistance and GMR contributions are distinguished at low temperature (i.e., 10 K) since the O-implanted areas become exchange coupled. This planar GMR is principally ascribed to the spatial modulation of coercivity in a spring-magnet-type configuration, which results in 180° Néel extrinsic domain walls at the Co/Co-CoO interfaces. The versatility, in terms of pattern size, morphology, and composition adjustment, of this method offers a unique route to fabricate planar systems for, among others, spintronic research and applications.

1. Introduction

Nowadays, spintronic research and devices are mainly based on vertical rather than planar systems, such as multilayered magnetic tunnel junctions.[1,2] That is, sandwich geometries (vertical multilayers) prevail over in-plane modulated patterns (lateral multilayers) since planar technology (e.g., planar giant magnetoresistance (GMR) readers)[3] still remains challenging from a fabrication point of view. The

Dr. E. Menéndez, H. Modarresi, C. Petermann, Prof. A. Vantomme, Prof. K. Temst
KU Leuven
Instituut voor Kern- en Stralingsfysica
Celestijnenlaan 200 D, 3001 Leuven, Belgium
E-mail: enricmenendez@gmail.com; kristiaan.temst@kuleuven.be
Prof. J. Nogués, Dr. N. Domingo
Catalan Institute of Nanoscience and Nanotechnology (ICN2)
CSIC and The Barcelona Institute of Science and Technology
Campus UAB
Bellaterra, 08193 Barcelona, Spain
E-mail: josep.nogues@uab.cat
Prof. J. Nogués
ICREA, Pg. Lluís Companys 23
08010 Barcelona, Spain
Dr. H. Liu, Prof. C. Van Haesendonck
KU Leuven
Laboratorium voor Vaste-Stoffysica en Magnetisme
Celestijnenlaan 200 D, 3001 Leuven, Belgium
Dr. B. J. Kirby
NIST Center for Neutron Research
National Institute of Standards and Technology
Gaithersburg, Maryland 20899, USA
Dr. A. S. Mohd, Dr. Z. Salhi, Dr. E. Babcock, Dr. S. Mattauch
Jülich Centre for Neutron Science (JCNS) at Heinz Maier-Leibnitz Zentrum (MLZ)
Forschungszentrum Jülich GmbH
85747 Garching, Germany

DOI: 10.1002/smll.201603465

preparation of lateral multilayers can be achieved, among others, by shadow evaporation techniques which combine lithography and multiple depositions,[4] lithography and a combination of hard and soft lift-off methods,[5] multilevel lithography and ion milling to introduce periodic thickness modulations which may result in magnetic lateral multilayers,[6–8] self-organization through chemical instabilities[9–11] or ion beam assisted deposition.[12,13] Although these methods ensure in-plane compositional and/or magnetic modulations, many of them suffer from different drawbacks like several intermediate fabrication steps, pattern size control, limited morphology design, or nontunable interfaces. Therefore, routes which can lead to lateral multilayers with sharp interfaces and versatility in pattern design using a minimal number of preparation steps are of great interest, not only from a technological point of view but also from a scientific side. Planar technology offers advantages compared to standard vertical technology (e.g., devices are finished at the wafer level)[3] and more flexibility to perform spatially resolved characterization due to its lateral geometry.[14] Interestingly, lateral magnetic multilayers have been proposed not only for spintronic purposes but also for other applications like magnonic crystals for GHz devices (e.g., filters or waveguides)[15,16] or magnetic encoders (e.g., for biomedical applications).[17,18] In this context, ion irradiation/implantation in combination with lithography has become a suitable method to obtain lateral multilayers[19–23] and magnetically pattern systems.[19,20,24,25]

Ion implantation is a suitable technique to controllably modify the near-surface of materials due to the limited range of penetration of ions,[26] turning out to be particularly convenient to tune the structure and composition of thin films. Light-ion irradiation (mainly of noble gases) of ferromagnetic (FM) thin films and multilayers has been used for the modification of magnetic properties, such as magnetic anisotropy, saturation magnetization, exchange coupling, or exchange bias.[27] Furthermore, irradiation using heavy ions and ion implantation have also been utilized with the aim to induce increased collisional damage and/or to create composition adjustments.[28] Recently, oxygen ion implantation has been confirmed as an advantageous route to form antiferromagnetic (AFM) oxides embedded in FM thin films (e.g., Co), giving rise to exchange bias.[29–34] In parallel, the wide variety of lithography techniques yields a high flexibility in pattern design and, thus, in shadow mask fabrication for ion implantation.

We have combined O ion implantation with UV lithography in order to prepare Co/Co-CoO microscale lines with laterally modulated magnetic properties, which give rise to planar GMR effects.

2. Results and Discussion

2.1. Preparation of Laterally Modulated Co/Co-CoO Micropatterns by Combining O Ion Implantation and Lithography

A Au-sandwiched Co thin film (i.e., 15 nm Au/30 nm Co/10 nm Au) was grown by molecular beam epitaxy onto a thermally oxidized Si (100) wafer. The top 15 nm thick Au layer (i.e., the capping layer) prevents Co from natural oxidation, while the bottom 10 nm thick Au layer (i.e., the buffer layer) is introduced to minimize the atomic intermixing between Co and SiO_2 upon implantation. Both Au layers are intended to avoid any source of CoO formation other than that induced by the O ion implantation. The Co layer is polycrystalline and consists of a mixture of face-centered cubic Co, hexagonal close-packed Co, and stacking faults. Upon oxygen implantation, the amount of crystalline metallic Co significantly decreases because of the increased density of defects within the Co layer and due to the CoO formation. The rather large fluence of 2×10^{17} ions cm^{-2} was chosen with the aim to considerably modify the target areas from structural and compositional points of view and, thus, to induce significant differences in the magnetic properties between the implanted and nonimplanted lines. The O incorporation into the Co layer (reaching around 29 at% of O at a half depth of the Co layer, **Figure 1**a)[35] occurs mainly via a grain boundary oxidation mechanism, as confirmed by the evolution of crystallite size with O ion implantation in similar Co thin films.[30] With ion implantation, the Co grain boundaries oxidize, leading to the growth of the CoO counterpart (58 at%).[32] Note that increasing the fluence would eventually lead to pure antiferromagnetic CoO patterned lines, which could probably result in effects like lateral exchange bias.[36]

Microscale patterns consisting of 1.6 µm wide lines with a period of 4 µm were prepared by UV lithography. Since the lithographed resist is intended to be used as a shadow mask for ion implantation, an additional Au layer of 20 nm was deposited onto the resist to further ensure the full stopping of the impinging ions by the resist during implantation (Figure 1b). The sample was then implanted with 45 keV O ions to a fluence of 2×10^{17} ions cm^{-2} and, afterward, the remaining resist stripped away (Figure 1c).

The TRIDYN[35] program was used to simulate the dynamic changes of thickness (i.e., interplay between sputtering and swelling) and composition (e.g., O depth distribution along the resist-free areas, Figure 1a). In such conditions, material removal prevails over swelling and it is estimated to be around 16 nm. Moreover, qualitative TRIM[37] simulations (not shown) confirm that the shadow mask (i.e., Au(20 nm)-resist(1.2 µm)) completely guarantees the full stopping of the incoming O ions (Figure 1c). In this way, the sample is selectively implanted, resulting in a periodic formation of CoO.[32] Hence, the combination of O ion implantation and lithography yields a laterally modulated pattern consisting of alternating Co and Co-CoO microscale lines sandwiched between Au layers (Figure 1c). As schematized in Figure 1c, the resulting topography is ascribed to the fact that the thickness of sputtered material (i.e., around 16 nm) upon implantation is lower than the extra 20 nm thick Au layer deposited onto the system prior to implantation.

2.2. Room Temperature Magnetic and Transport Properties

Figure 2a,b shows the longitudinal and transversal magneto-optic Kerr effect (MOKE) measurements, respectively, along

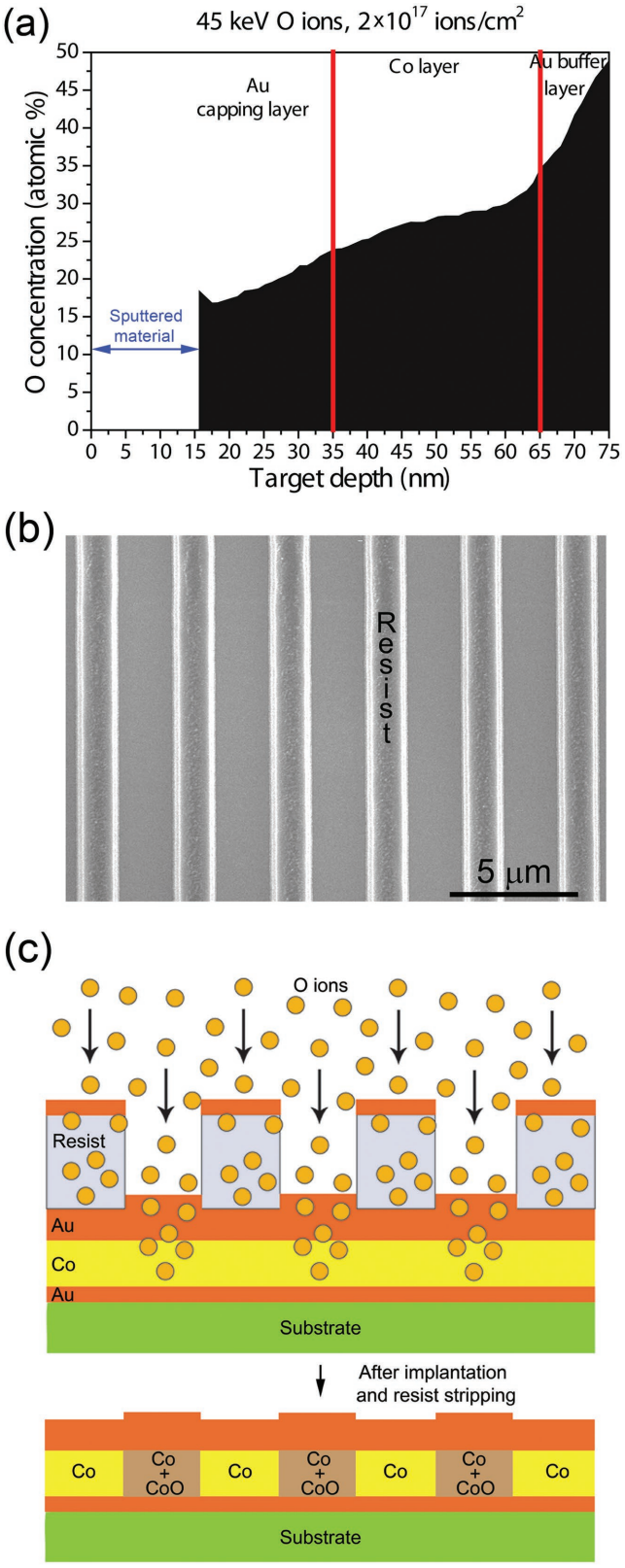

Figure 1. a) O depth profile along sample depth of the areas without resist, simulated by TRIDYN,[36] for 45 keV O ions and a fluence of 2×10^{17} ions cm^{-2}. The vertical red lines are schematic guides, since, at such fluence, atomic intermixing is significant and the interfaces between layers become blurred. b) Scanning electron microscopy image, taken with secondary electrons, of the lithographed resist mask after the deposition of the additional Au layer. c) Cartoon showing the implantation process and the cross section view of the laterally modulated microscale lines in which Co and Co-CoO areas are alternating.

and across the lines. The longitudinal MOKE measurement along the lines reveals a double-step-like hysteresis loop. This is the result of the interplay between the dissimilar coercivities of the nonimplanted and implanted areas (the implanted lines being magnetically harder) and dipolar interactions,[38] which tend to stabilize the antiparallel alignment of adjacent lines once the magnetization of the soft areas (i.e., nonimplanted lines) is switched. The implantation leads to an increase in the number of defects in Co, such as stacking faults, that can act as pinning centers for magnetization reversal, resulting in an enhanced coercivity.[32,39] Upon implantation, oxygen primarily accumulates at the grain boundaries forming CoO, reducing the grain size, and thus isolating the Co grains. This might also yield decreased exchange interactions between Co grains leading to an increased coercivity. Furthermore, the implantation-induced increase of coercivity can also be partially ascribed to exchange interactions between the Co grains and the CoO at the grain boundaries.[32,40] Conversely, the longitudinal MOKE measurement across the lines shows a single-step hysteresis loop with slightly decreased coercivity and remanence, evidencing traces of shape anisotropy. In this case, once the magnetization of the pure Co lines is switched, the dipolar fields favor the reversal of the implanted areas, softening the jumps in magnetization and thus yielding a more gradual magnetization reversal. As can be seen in Figure 2b, the transversal MOKE measurement along the lines reveals traces of perpendicular magnetization upon reversal, indicating that coherent rotation is an active magnetization reversal mechanism. The slightly broadened transversal signal for the measurement across the lines confirms the mild shape anisotropy already observed by longitudinal MOKE, since coherent rotation typically governs the magnetization reversal along hard axes.[41]

Magnetoresistance, $\Delta R/R$, with the current and external magnetic field applied along the patterned lines exhibits an overall positive effect (Figure 2c) for both descending and ascending branches. Lorentz magnetoresistance, originating from the deflection of the current lines inside magnetic domains, and the magnetoresistance effect linked to the twisting of the current lines at the domain walls (i.e., Hall effect contribution) can be neglected due to the polycrystalline nature of the sample.[42] Thus, the observed $\Delta R/R$ might at first glance be ascribed to anisotropic magnetoresistance (AMR), which arises from spin–orbit coupling. However, in this configuration, AMR contributions should result in a decrease of the resistance regardless of the magnetization reversal mechanism since the change in AMR is proportional to $\cos^2\theta$, where θ is the angle between the current and the magnetization.[43] Hence, this implies that, in the Co/Co-CoO lateral multilayers, AMR is overcome by another magnetoresistance effect. The maxima of magnetoresistance appear for an applied magnetic field between –7 and 7 mT. As can be seen in the longitudinal MOKE measurement along the lines (Figure 2a), the soft magnetic areas (i.e., nonimplanted) reverse their magnetization in this field range, whereas the

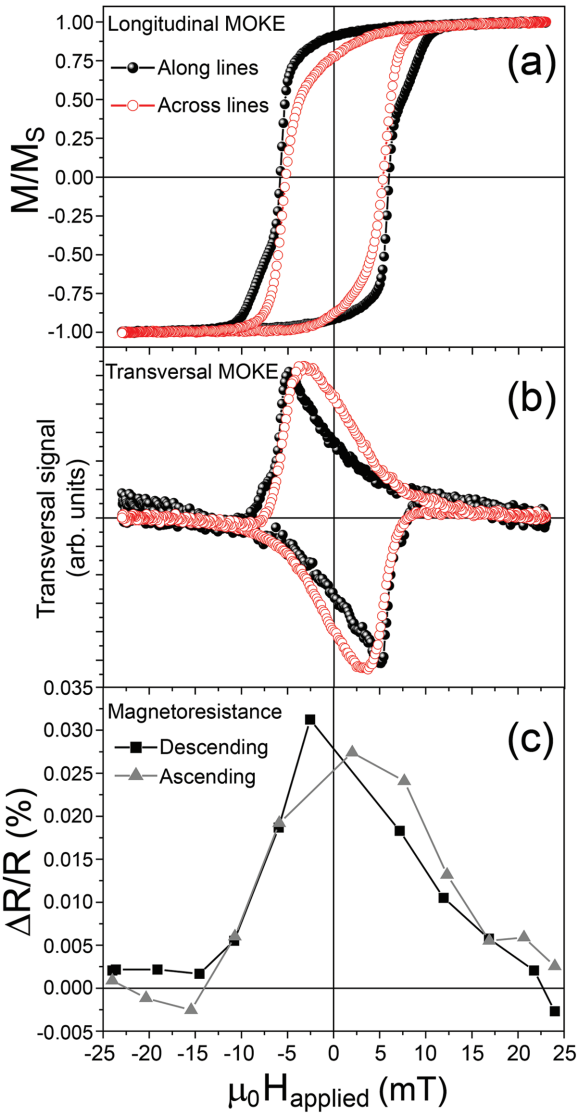

Figure 2. a) and (b) are the longitudinal and non-normalized transversal magneto-optic Kerr effect (MOKE) measurements, respectively, along and across the lines. c) is the magnetoresistance measurement with the current and magnetic field applied along the lines. All measurements were performed at room temperature.

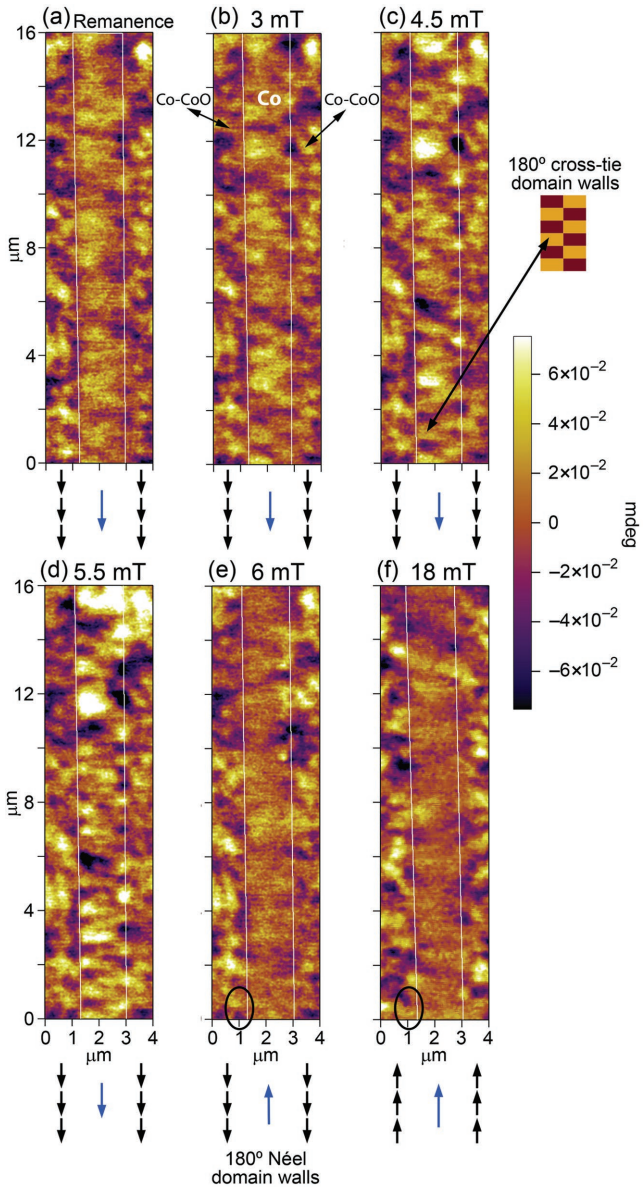

Figure 3. Room temperature magnetic force microscopy (MFM) images at remanence after saturating the sample along the lines in a field of a) −100 mT and at increasingly positive applied magnetic fields along the lines of b) 3, c) 4.5, d) 5.5, e) 6, and f) 18 mT. Below each panel, a cartoon of the main orientation of the magnetization of the lines is presented. The white lines are guides to the eye and highlight the borders of the characterized pure Co line. The ellipses drawn in panels (e) and (f) indicate the magnetization reversal of the implanted areas.

magnetization of the implanted lines remains essentially unaltered. To further unravel the magnetic domain configurations upon magnetization reversal, magnetic force microscopy (MFM) images were taken at remanence (after saturating the sample along the lines in a field of −100 mT) and at increasingly positive applied magnetic fields along the lines (**Figure 3**). Figure 3a, taken at remanence, reveals a multidomain magnetic structure of the pure Co lines in agreement with the longitudinal MOKE characterization, this shows that the remanence is lower than the saturation magnetization. Upon increasing the applied magnetic field while keeping the main orientation of the magnetization of the nonimplanted areas unchanged (Figure 3b–d), the multidomain structure reinforces and 180° cross-tie domain walls (domain walls which contain both Néel- and Bloch-like counterparts)[44–47] can be locally observed within the O-free Co lines. As can be seen in Figure 3d,e, the switch of the main orientation of the magnetization takes place in an applied magnetic field interval of less than 0.5 mT in fair concordance with the narrow switching field range of the nonimplanted lines (Figure 2a). Differences in applied magnetic field dependences among MOKE, magnetoresistance and MFM characterization are mainly ascribed to the local probing character of these techniques. Upon switching of the soft magnetic parts, Néel-like domain walls[48] at the Co/Co-CoO interfaces (see the magnetization configuration scheme of Figure 3e) are envisaged until the implanted areas fully reverse. This indicates that, during and after the magnetization reversal of the pristine Co areas, a local antiparallel

alignment of the magnetization (via 180° cross-tie- and interface 180° Néel-like domain walls, respectively) is present. These interface 180° Néel-like domain walls have already been reported, among others, in Co-based[49] and Fe-based[50–52] systems. Therefore, taking into account this local antiparallel configuration, the observed positive magnetoresistance (Figure 2c) can be linked to a domain wall resistance effect ruled by giant magnetoresistance mechanisms.[49,53] Since domain walls in single Co thin films do not significantly scatter conduction electrons (i.e., GMR effects are not the dominant source of magnetoresistance),[54] this confirms the high density of domain walls achieved in this system, which is ascribed to both intrinsic (e.g., magnetocrystalline anisotropy of Co) and extrinsic (e.g., pattern design, Co thickness, shape anisotropy, etc.) magnetic properties. Both descending and ascending branches exhibit a magnetoresistance maximum, suggesting that the formation of these 180° domain walls is, to some extent, reversible. The maximum variation with respect to the resistance at saturation is approximately $\Delta R/R$ (%) = 0.03, i.e., an order of magnitude which is consistent with the domain wall resistance of other Co-based systems.[49] Although the measured effects are unambiguous, the $\Delta R/R$ values are perhaps lower than one would expect, this can be attributed to the fact that they are somewhat limited by the shunting effects of the Au capping and buffer layers and also by the difference in resistance between the Co and Co-CoO lines (which tends to favor the flow of current through the Co layer).

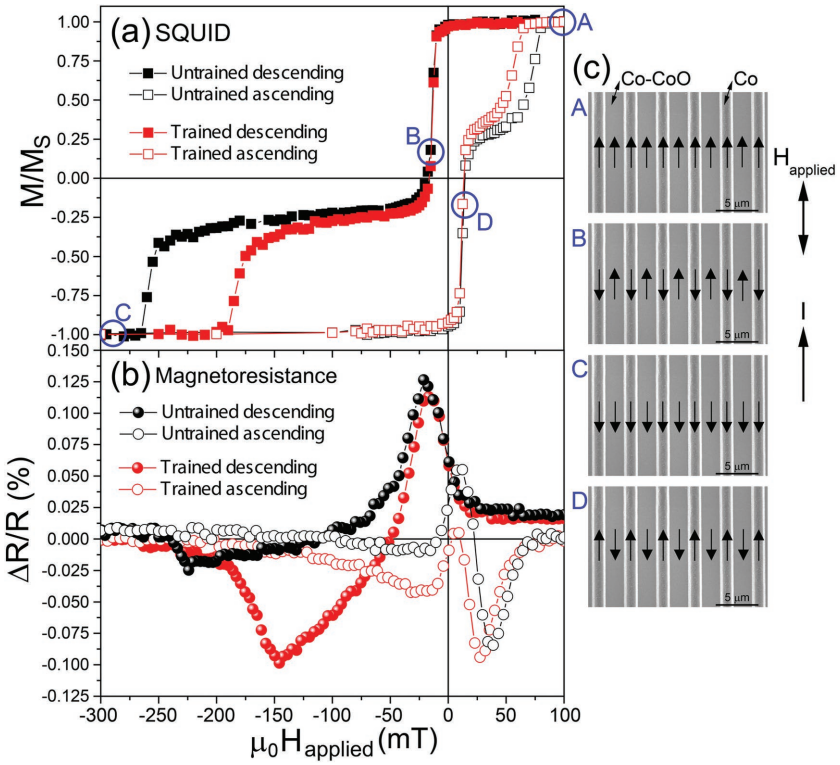

Figure 4. a) Untrained and trained superconducting quantum interference device (SQUID) magnetization measurements along the lines. b) Untrained and trained magnetoresistance measurements with the current and applied magnetic field along the lines and c) cartoon showing the magnetization configuration at particular applied magnetic fields. B and D represent stripe domains with 180° Néel domain walls at the interfaces. All measurements were performed at 10 K after field cooling from room temperature in a magnetic field of 800 mT applied parallel to the lines.

The results indicate that the lateral magnetic modulation is an excellent playground to manipulate the magnetization reversal and the domain structure,[6,21] leading to novel effects.

2.3. Low Temperature Magnetic and Transport Properties

For the low temperature characterization (i.e., magnetometry, magnetoresistance and polarized neutron reflectometry (PNR)), the sample was cooled from room temperature down to 10 K in a magnetic field of 800 mT applied along the lines. **Figure 4**a shows the superconducting quantum interference device (SQUID) magnetization measurements of consecutively measured hysteresis loops (i.e., untrained and trained) along the lines. These double-step cycles are the result of a combination of soft and hard magnetic contributions, which originate from the pure Co and the O-implanted lines, respectively. In contrast to room temperature, the coercivity of the O-implanted Co lines is significantly enhanced. Together with the pronounced exchange bias shift[55–57] (around –92.7 mT), this confirms that the Co and the CoO in the implanted areas are exchange coupled, in agreement with previously reported results.[32,34] The trained loop shows a decreased exchange bias shift of –62.8 mT in concordance with the strong training effects that occur in Co-CoO systems.[34] Remarkably, this lateral configuration of exchange-biased (Co-CoO) and nonbiased (Co) alternating regions gives rise to a well-defined spatially modulated coercivity. The exchange bias shift and coercivity are not significantly different from those of nonpatterned samples implanted using similar conditions. In general, with O ion implantation, both exchange bias shift and coercivity increase with fluence and, hence, with O concentration until reach a type of steady state.[32,34] It is important to emphasize that we have used the knowledge gathered in the nonpatterned samples[30–34] to design the patterned films, since, for the sizes used in the patterning, the magnetic properties are virtually the same.

As can be seen in Figure 4b, parallel magnetoresistance (i.e., current and $H_{applied}$ along the lines) shows traces of positive and negative contributions for both untrained and trained branches. Whereas the maxima appear in the field range where the nonimplanted areas reverse, the minima emerge in the field region corresponding to the reversal of O-implanted areas. With consecutively measured loops, the positive contributions remain virtually unaltered, while the

minima are located at decreased applied magnetic fields, evidencing training[55,56] and, thus, indicating that the negative contributions originate from the implanted areas which are exchange coupled. In the second measurement (i.e., trained), the depth of the minimum is somewhat increased due to minor spin rotation traces arising from training.[34] In any case, as can be seen below, domain wall nucleation and motion remains as the main reversal mechanism.

To further shed light on this magnetoresistance behavior, the magnetization reversal mechanisms have been investigated by PNR with off-specular analysis. The PNR magnetic field scans acquired by integrating the full signal (i.e., specular and off-specular) are presented in **Figure 5**. In the field region where the implanted areas inverse their magnetization, no spin flip (SF) signal (ud and du) above the background level can be observed, indicating that the magnetization reversal is mainly ruled by domain wall nucleation and motion, similar to the case of homogeneously implanted Co thin films.[34] Conversely, a large spin flip signal is detected in the field range where the pristine Co lines reverse. The corresponding nonspin flip (NSF) signals (uu and dd) cross roughly halfway between the minimum and maximum values, suggesting the existence of another source of spin flip signal on top of that arising from coherent rotation. The disentanglement of the specular and off-specular signals in the magnetic field scans (not shown) indicates that most of the spin flip signal arises from diffuse (i.e., off-specular) magnetic scattering (i.e., resulting from in-plane magnetic correlations). This is consistent with a magnetization reversal of the Co lines governed by domain wall nucleation and motion with coherent rotation traces, in agreement with the room temperature transversal MOKE characterization.

Figure 6 shows the α_i–α_f maps of the reflected intensity corresponding to uu (a), dd (b), ud (c), and du (d) neutrons, recorded in an applied magnetic field of –0.6 mT. This value was chosen with a twofold aim. That is, to avoid depolarization of the neutron beam (see the Experimental Section) and to investigate the remnant state of the O-free Co areas where, as can be seen in Figure 4, the magnetization of the Co areas has partially reversed ($M_R < M_S$, with M_R and M_S the magnetization at remanence and at saturation, respectively), allowing the study of the magnetization reversal of the O-free Co areas. The off-specular fringes of the nonspin flip signals (panels (a) and (b)) confirm the high lateral topographic correlation of the sample, while the off-specular signal of the spin flip maps reveal in-plane magnetic correlations, in concordance with the large spin flip signal observed in the magnetic field scans of Figure 5. This is in agreement with previously reported off-specular PNR results on Co thin films where lateral networks of Néel domain walls are also responsible for the off-specular signal.[58] The asymmetry (i.e., spin dependence) in the diffuse spin flip scattering, where ud does not equal du, is ascribed to a birefringence phenomenon.[59–62] Since the measurements were conducted in only 0.6 mT, Zeeman splitting originating from the applied field is ruled out as a source of off-specular spin-flip signal.[63–65] Conversely, in the field range where the magnetization of the implanted areas reverses and beyond (i.e., saturation), no traces of off-specular signal are observed, indicating no

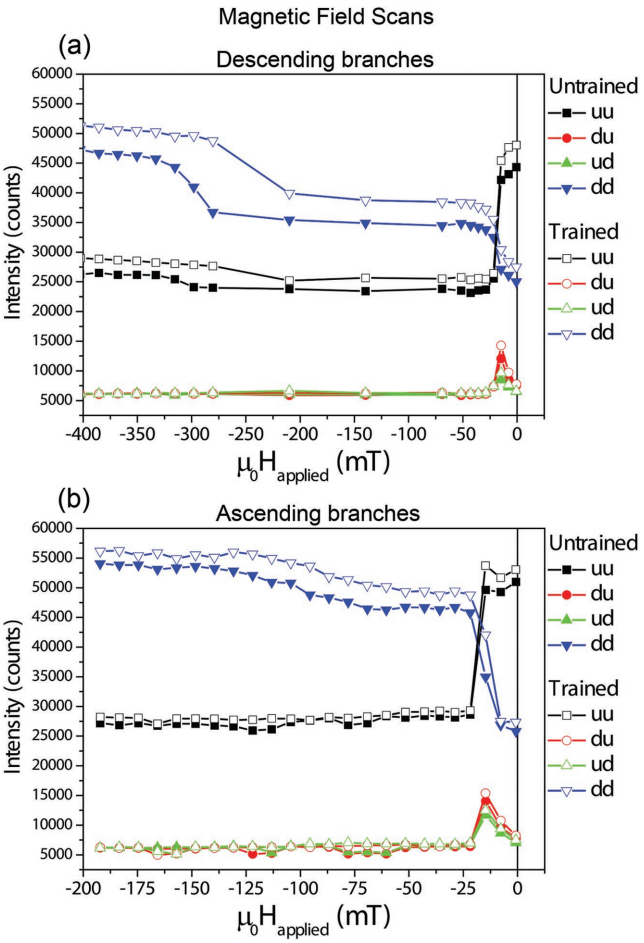

Figure 5. Polarized neutron reflectometry magnetic field scans along the lines of the untrained and trained descending a) and ascending b) branches of the hysteresis loops. These measurements show the integrated (specular + off-specular signals) raw data. All measurements were performed at 10 K after field cooling from room temperature in a magnetic field applied parallel to the lines of +800 and –800 mT for the descending and ascending branches, respectively (see the Experimental Section for further details).

in-plane magnetic correlations and, therefore, suggesting that domain walls with partial or antiparallel alignment are much scarcer or negligible with respect to the pure Co areas. These results were corroborated by similar observations in PNR measurements of nonpatterned films. This is in agreement with the fact that AMR prevails over GMR as the dominant source of magnetoresistance in the implanted areas. Taking this into account, the small negative contribution to the magnetoresistance of the untrained descending branch (Figure 4b) can be explained by weak AMR effects originating from minor perpendicular contributions of the magnetization during domain wall nucleation and motion. This negative resistance contribution becomes slightly more pronounced with consecutive reversals (training), suggesting that coherent rotation to some extent reinforces since the corresponding perpendicular components of the magnetization are significantly larger (being largest at the coercive fields) than those of domain wall nucleation and motion processes. Even though this evolution could be thought to be consistent with the reversal mechanism asymmetry in Co/CoO bilayers

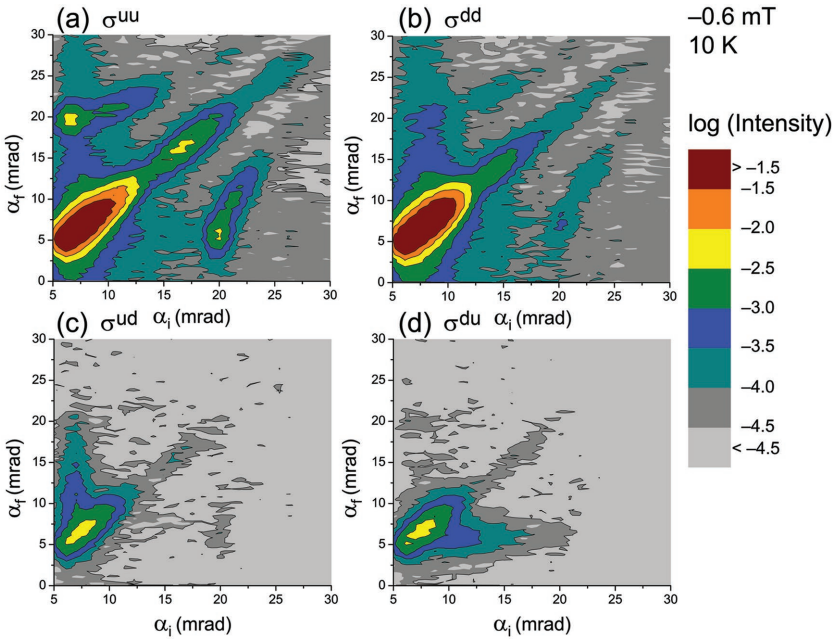

Figure 6. Polarized neutron reflectometry α_i–α_f maps corresponding to a) σ^{uu}, b) σ^{dd}, c) σ^{ud}, and d) σ^{du} scattering cross-sections, taken at 10 K in a magnetic field of –0.6 mT applied along the lines. The scattering cross-sections σ^{uu}, σ^{dd}, σ^{ud}, and σ^{du} are the result of correcting, for polarization, polarization analysis and flipping inefficiencies, the raw measured reflectivities uu, dd, ud, and du, respectively. The measurements were performed after field cooling from room temperature in a magnetic field of 800 mT applied parallel to the lines.

and O-implanted systems with low O contents, these negative contributions are weak (0.11% for the trained descending branch), in concordance with the PNR results which indicate that the reversals of implanted areas are mainly ruled by domain wall nucleation and motion (Figure 5). In fact, reversals fully taking place via coherent rotation would lead to much more pronounced changes in resistance, as it happens in Co/CoO bilayers where magnetoresistance differences up to 80% are observed.[66] On the contrary, in the field range where the Co lines inverse their magnetization, the resistance exhibits an upturn rather than showing a decrease, which screens any AMR effects arising from domain wall nucleation and motion and coherent rotation traces. As can be seen in Figure 4b, this increase is already significant where most of the magnetization has not yet reversed (remanence is above 92% for the first four reversals, Figure 4a), in consonance with the existence of intrinsic 180° cross-tie domain walls within the Co areas. As it happens at room temperature, these incipient positive magnetoresistance effects can be linked to domain wall resistance contributions through a giant magnetoresistance mechanism.[49,53] Nonetheless, the maxima of spin flip signal occur when the magnetization of the Co areas is half reversed (i.e., at the coercive fields, Figure 5), whereas the magnetoresistance reaches its maximum when the Co areas are fully reversed (i.e., at around –16 mT for the descending branches). This implies the existence of a major source of positive magnetoresistance which can be linked to the 180° Néel-like domain walls arising from the antiparallel alignment at the interface of adjacent lines upon reversal of the soft areas (Figure 4c). Namely, the antiparallel coupling results in 180° Néel-like domain walls at the Co/Co-CoO interfaces and it consequently yields an additional increase of the resistance due to a giant magnetoresistance mechanism. In contrast to the intrinsic Néel domain walls arising from the magnetization reversal of Co lines, these interfacial domain walls are of extrinsic origin (i.e., artificial) since they originate from the magnetic periodicity coming from the dissimilar coercivity of contiguous lines. Actually, this also applies to the room temperature magnetoresistance, whose interpretation is less straightforward since the magnetic contributions of nonimplanted and implanted lines are more entangled due to the smaller difference in coercive fields. The positive contribution reaches values with respect to the resistance at saturation up to around $\Delta R/R\,(\%) = 0.13$, close to four times larger than at room temperature, evidencing the partial disentanglement of the AMR contribution ascribed to exchange-coupled areas. These magnetoresistance maxima appear in both descending and ascending branches and do not suffer from training, indicating a high reversibility in the formation of these 180° domain walls. Remarkably, for continuously implanted samples (i.e., nonpatterned), the effective magnetoresistance behavior is ruled by AMR effects,[29] confirming that the observed GMR character is intimately linked to the lateral multilayer structure.

3. Conclusion

Ion implantation through lithographed masks is shown to be an advantageous method to prepare laterally (compositionally and magnetically) modulated samples with tunable giant magnetoresistance and potential uses for, among others, spintronic research and applications. A lateral microscale pattern consisting of alternating Co (1.6 μm wide) and Co-CoO (2.4 μm wide) lines has been prepared by oxygen ion implantation into a prelithographed Au-sandwiched Co thin film. The lithography is used to obtain a shadow mask for ion implantation. By locally implanting O into a Co thin film, the magnetic properties can be periodically altered in the plane of the sample, e.g., in our case, a spatially modulated coercivity is achieved. Consequently, domain structures can be imposed by the application of well-defined magnetic fields. This magnetic periodicity leads to an overall positive giant magnetoresistance behavior at room temperature, while anisotropic and giant magnetoresistance contributions are distinguished at low temperature since the O-implanted areas become exchange coupled. This planar giant magnetoresistance is primarily ascribed to the spatial modulation of coercivity (in a spring-magnet-type configuration), which results in 180° Néel-like domain walls at the Co/Co-CoO interfaces. This novel approach may constitute an important

asset for planar spintronics and other magnetic lateral multilayer applications. From a technological point of view, it is worth noting that any implantation brings about an intrinsic lateral range of stochastic origin.[26] Taking into account the current conditions, the lateral range of implanted ions in the Co layer is roughly 25 nm (estimated from TRIM[37] simulations, see Figure S1, Supporting Information). Therefore, the miniaturization limit (i.e., minimum width of the lines) for this approach would be set around 50 nm, although this could be reduced by carefully designing the structure of the multilayer and the implantation conditions. However, this limit could be reduced by controllably modifying the local microstructure through annealing procedures.[33] Nonetheless, this constitutes the first report on the use of O ion implantation to produce patterned exchange bias systems. In fact, by carefully optimizing the implanting conditions,[32] we can tune the amount of CoO in the implanted areas and, consequently, locally change the magnetic properties of the patterns from soft ferromagnetic to hard ferromagnetic, or even antiferromagnetic (i.e., destroying its ferromagnetic character).

4. Experimental Section

A 1.5×1.5 cm^2 Au-sandwiched polycrystalline 30 nm thick Co thin film (i.e., 15 nm Au/30 nm Co/10 nm Au) was grown by molecular beam epitaxy at room temperature on thermally oxidized Si (100) substrates (450 nm thick SiO_2). All layers were grown at a pressure of around 3×10^{-10} mbar. The Co layer consists of a mixture of face-centered cubic Co, hexagonal close-packed Co and stacking faults.[32]

UV lithography was used to design microscale lines on top of the sample. In order to achieve a fine undercutting of the resist profile, a nonphotosensitive layer (Shipley, MICROPOSIT LOL2000) was first spin coated onto the sample for 50 s at 4000 rpm, resulting in a thickness of around 0.16 µm. Next, the sample was soft baked for 5 min at 115 °C. Subsequently, a photosensitive layer (Shipley, MICROPOSIT S1813) was spin coated on top of the first resist for 50 s at 5000 rpm, yielding a total thickness of ≈1.2 µm. The resist system was then soft baked at 115 °C for 1 min. The sample was afterward subjected to illumination through a predesigned mask consisting of 2 µm wide lines with a period of 4 µm with UV light from a short-arc mercury vapor lamp (Osram, HBO 200W/4). The time of exposure was about 10 s. The exposed sample was then submerged into a developer solution (Shipley, MICROPOSIT MF319), which dissolved the illuminated parts of the resist layer (positive resist). Since the development rate of the underlying LOL2000 layer was higher than that of the S1813 resist and the nonphotosensitive LOL2000 layer dissolves in a controllable way, well defined and reproducible undercuts of the top resist layer could be achieved. The development time was 30 s. While developing, the exposed resist was removed and dissolution of the photoresist slows down, but the developer continued to dissolve the LOL2000 layer in the open areas and under the resist edge, leading to well-defined structures. The dimensions of the pattern were determined by optical microscopy, indicating the formation of 1.6 µm wide lines with a period of 4 µm (the lines constitute 40% of the sample surface and the noncovered areas 60%).

Subsequently, with the aim to further increase the thickness of the resist layer, 20 nm Au was additionally sputtered on top. The lithographed sample was then implanted using 45 keV O ions to a fluence of 2×10^{17} ions cm^{-2}.

The magnetic properties were investigated, at room temperature, by means of MOKE measurements and, at low temperature, by SQUID magnetometry. With the aim to probe several lines, the laser of the MOKE setup was defocused up to 50 µm in diameter. MFM with in situ applied magnetic field was used to further unravel the magnetization reversal at room temperature.

High-resolution four-terminal magnetoresistance measurements were performed both at room temperature and at 10 K (after field cooling from room temperature in a magnetic field of 800 mT applied parallel to the lines) in a helium flow cryostat by integrating the sample into an Adler–Jackson bridge. The AC measuring current for the lock-in detection had a frequency of 27.7 Hz and a root-mean-square amplitude of 3.5 A. The current direction was established along the lines.

Primary PNR measurements were carried out at the MARIA instrument, operated by JCNS at the Heinz Maier-Leibnitz Zentrum (MLZ), Garching, Germany. A neutron wavelength of 6 Å was used. Specifically, PNR magnetic field scans were carried out to unravel the magnetization reversal mechanisms along the lines at low temperature after parallel field cooling. From the specular polarized reflectivity pattern recorded in the saturated magnetization state, the angle (i.e., the incidence angle of neutrons) showing a good tradeoff between intensity and splitting ratio among nonspin flip signals was selected to perform magnetic field scans. That is, at a certain fixed angle (i.e., 16.8 mrad (0.035 Å^{-1})), the NSF and the SF signals were recorded as a function of the applied magnetic field.[67,68] Upon reflection, the neutron polarization was analyzed, resulting in four different measured reflectivities: two NSF signals, uu and dd, and two SF signals, ud and du. The first index denoted the polarization prior to reflection and the second index the polarization after reflection. In order to maintain the polarization of the neutrons throughout the reflectometer, guide fields were mounted at dedicated positions. Since neutrons depolarized due to stray fields when a positive field was applied, the measurements could only be performed at negative fields. Hence, in order to assess the ascending branches of the hysteresis loops (which usually lied at positive fields after positive field cooling), the sample was cooled in a negative field, implying that the aforementioned ascending branches would then reside at negative fields. The ascending and descending branches were in fact measured after separate field cooling processes, which explained why the magnetic field scans always had a negative magnetic field scale. Moreover, 2D reflectivity measurements (α_i–α_f maps containing the specular and off-specular signals) were performed at dedicated applied magnetic fields (Figure 6). The polarized and analyzed data of Figure 6 were corrected according to Ref. [69] after taking into account that MARIA was equipped with a polarizing supermirror (double bounce) as a polarizer and an in situ SEOP (Spin-Exchange Optical Pumping) ^{3}He-filter as an analyzer.[70] The latter was combined with a momentary transverse radio frequency (RF)-field that could perform an adiabatic fast passage spin reversal of the ^{3}He and was used instead of a separate neutron spin flipper after the sample. In this way, the analyzer had in both directions the same efficiency. Since the ^{3}He-filter was polarized in situ, time-dependent corrections were generally not needed and its analyzing power

was ≈ 98% for the wavelength used. On the side of the polarizer, the neutrons were flipped with a RF-flipper which was working close to 100% and the incident polarization is 98%. Hence, the data shown in Figure 6 were corrected for the incident beam polarization, the small incident beam flipping inefficiency, and the ^{3}He analyzing power removing the leakage in the spin flip channels. In fact, the processed data showed the σ^{uu}, σ^{dd}, σ^{ud}, and σ^{du} scattering cross-sections which, in the limit of ideal polarization and flipping efficiencies, equaled to the uu, dd, ud, du reflectivity measurements, respectively. Secondary PNR measurements on unpatterned films were performed using the PBR (Polarized Beam Reflectometer) beamline at the NIST Center for Neutron Research.

Supporting Information

Supporting Information is available from the Wiley Online Library or from the author.

Acknowledgements

This work was financed by the Research Foundation-Flanders (FWO), the Concerted Research ActionGOA/14/007, the 2014-SGR-1015 project of the Generalitat de Catalunya, and the European Commission under the 7th Framework Programme through the "Research Infrastructure" action of the "Capacities" Programme, NMI3-II Grant No. 283883. This work is based upon experiments (Proposal Nos. 5928 and 9384) performed at the MARIA instrument operated by JCNS at Heinz Maier-Leibnitz Zentrum (MLZ), Garching, Germany. The authors would like to thank IMEC for access to its lithography facilities as well as J. Moonens and J. Loo for technical support. ICN2 acknowledges support from the Severo Ochoa Program (MINECO, Grant SEV-2013-0295). Finally, the authors thank J. A. Borchers and B. B. Maranville for fruitful discussions and J. England of Applied Materials (UK) for the assistance in performing the TRIDYN simulations.

[1] I. Zutic, J. Fabian, S. D. Sarma, *Rev. Mod. Phys.* **2004**, *76*, 323.
[2] S. D. Bader, S. S. P. Parkin, *Annu. Rev. Condens. Matter Phys.* **2010**, *1*, 71.
[3] E. D. Tober, R. F. Marks, D. D. Chambliss, K. P. Roche, M. F. Toney, A. J. Kellock, R. F. C. Farrow, *Appl. Phys. Lett.* **2000**, *77*, 2728.
[4] T. Kimura, T. Sato, Y. Otani, *Phys. Rev. Lett.* **2008**, *100*, 066602.
[5] A. O. Adeyeye, M. K. Husain, V. Ng, *J. Magn. Magn. Mater.* **2002**, *248*, 355.
[6] A. Hierro-Rodriguez, G. Rodríguez-Rodríguez, J. M. Teixeira, G. N. Kakazei, J. B. Sousa, M. Vélez, J. I. Martín, L. M. Alvarez-Prado, J. M. Alameda, *J. Phys. D: Appl. Phys.* **2013**, *46*, 345001.
[7] A. Hierro-Rodriguez, M. Vélez, R. Morales, N. Soriano, G. Rodríguez-Rodríguez, L. M. Álvarez-Prado, J. I. Martín, J. M. Alameda, *Phys. Rev. B* **2013**, *88*, 174411.
[8] A. Hierro-Rodriguez, R. Cid, M. Vélez, G. Rodriguez-Rodriguez, J. I. Martín, L. M. Álvarez-Prado, J. M. Alameda, *Phys. Rev. Lett.* **2012**, *109*, 117202.
[9] E. D. Tober, R. F. C. Farrow, R. F. Marks, G. Witte, K. Kalki, D. D. Chambliss, *Phys. Rev. Lett.* **1998**, *81*, 1897.
[10] B. Borca, O. Fruchart, C. Meyer, *J. Appl. Phys.* **2006**, *99*, 08Q514.
[11] a) I. Golvano-Escobal, B. Özkale, S. Suriñach, M. D. Baró, T. Dobrovolska, I. Krastev, S. Pané, J. Sort, E. Pellicer, *J. Mater. Chem. C* **2014**, *2*, 8259; b) I. Golvano-Escobal, J. C. Gonzalez-Rosillo, N. Domingo, X. Illa, J. F. López-Barberá, J. Fornell, P. Solsona, L. Aballe, M. Foerster, S. Suriñach, M. D. Baró, T. Puig, S. Pané, J. Nogués, E. Pellicer, J. Sort, *Sci. Rep.* **2016**, *6*, 30398.
[12] M. Krause, A. Muecklich, T. W. H. Oates, M. Zschornak, S. Wintz, J. L. Endrino, C. Baehtz, A. Shalimov, S. Gemming, G. Abrasonis, *Appl. Phys. Lett.* **2012**, *101*, 053112.
[13] G. Abrasonis, K. Morawetz, *Phys. Rev. B* **2012**, *86*, 085452.
[14] J. P. Nozières, E. Saporito, B. Viala, *J. Magn. Magn. Mater.* **2002**, *341*, 242.
[15] B. Obry, P. Pirro, T. Brächer, A. V. Chumak, J. Osten, F. Ciubotaru, A. A. Serga, J. Fassbender, B. Hillebrands, *Appl. Phys. Lett.* **2013**, *102*, 202403.
[16] G. Gubbiotti, S. Tacchi, M. Madami, G. Carlotti, A. O. Adeyeye, M. Kostylev, *J. Phys. D: Appl. Phys.* **2010**, *43*, 264003.
[17] K. N. Vyas, B. Hong, J. F. K. Cooper, J. J. Palfreyman, C. H. W. Barnes, *IEEE Trans. Magn.* **2011**, *47*, 1571.
[18] D. M. Love, K. N. Vyas, A. Fernández-Pacheco, J. Llandro, J. J. Palfreyman, T. Mitrelias, C. H. W. Barnes, *RSC Adv.* **2015**, *5*, 10211.
[19] C. Chappert, H. Bernas, J. Ferre, V. Kottler, J. P. Jamet, Y. Chen, E. Cambril, T. Devolder, F. Rousseaux, V. Mathet, H. Launois, *Science* **1998**, *280*, 1919.
[20] C. Choi, K. Noh, D. Choi, J. Khamwannah, C. H. Liu, D. Hong, L. H. Chen, S. H. Jin, *IEEE Trans. Magn.* **2012**, *48*, 3402.
[21] N. Martin, I. Mönch, R. Schäfer, J. Fassbender, L. Schultz, J. McCord, *Phys. Rev. B* **2011**, *83*, 174423.
[22] B. Obry, T. Meyer, P. Pirro, T. Brächer, B. Lägel, J. Osten, T. Strache, J. Fassbender, B. Hillebrands, *Appl. Phys. Lett.* **2013**, *102*, 022409.
[23] R. Bali, S. Wintz, F. Meutzner, R. Hübner, R. Boucher, A. A. Ünal, S. Valencia, A. Neudert, K. Potzger, J. Bauch, F. Kronast, S. Facsko, J. Lindner, J. Fassbender, *Nano Lett.* **2014**, *14*, 435.
[24] E. Menéndez, J.-C. Stinville, C. Tromas, C. Templier, P. Villechaise, J.-P. Rivière, M. Drouet, A. Martinavičius, G. Abrasonis, J. Fassbender, M. D. Baró, J. Sort, J. Nogués, *Appl. Phys. Lett.* **2010**, *96*, 242509.
[25] E. Menéndez, J. Sort, M. O. Liedke, J. Fassbender, T. Gemming, A. Weber, L. J. Heyderman, S. Suriñach, K. V. Rao, S. C. Deevi, M. D. Baró, J. Nogués, *Small* **2009**, *5*, 229.
[26] M. Nastasi, J. W. Mayer, J. K. Hirvonen, *Ion-Solid Interactions: Fundamentals and Applications*, Cambridge University Press, Cambridge, USA **1996**.
[27] J. Fassbender, D. Ravelosona, Y. Samson, *J. Phys. D: Appl. Phys.* **2004**, *37*, R179.
[28] J. Fassbender, J. McCord, *J. Magn. Magn. Mater.* **2008**, *320*, 579.
[29] J. Demeter, J. Meersschaut, F. Almeida, S. Brems, C. Van Haesendonck, A. Teichert, R. Steitz, K. Temst, A. Vantomme, *Appl. Phys. Lett.* **2010**, *96*, 132503.
[30] J. Demeter, E. Menéndez, A. Vantomme, K. Temst, *J. Appl. Phys.* **2011**, *110*, 123902.
[31] J. Demeter, E. Menéndez, A. Schrauwen, A. Teichert, R. Steitz, S. Vandezande, A. R. Wildes, W. Vandervorst, K. Temst, A. Vantomme, *J. Phys. D: Appl. Phys.* **2012**, *45*, 405004.
[32] E. Menéndez, J. Demeter, J. Van Eyken, E. Jedryka, M. Wójcik, P. Nawrocki, J. Nogués, J. F. Lopez-Barbera, A. Vantomme, K. Temst, *ACS Appl. Mater. Interfaces* **2013**, *5*, 4320.
[33] E. Menéndez, H. Modarresi, T. Dias, J. Geshev, L. M. C. Pereira, K. Temst, A. Vantomme, *J. Appl. Phys.* **2014**, *115*, 133915.
[34] E. Menéndez, T. Dias, J. Geshev, J. F. Lopez-Barbera, J. Nogués, R. Steitz, B. J. Kirby, J. A. Borchers, L. M. C. Pereira, A. Vantomme, K. Temst, *Phys. Rev. B* **2014**, *89*, 144407.

[35] a) W. Möller, W. Eckstein, *Nucl. Instrum. Methods Phys. Res., Sect. B* **1984**, *2*, 814; b) TRIDYN_HZDR, https://www.hzdr.de/db/Cms?pOid=21578&pNid=0, (accessed October 2016).
[36] X. M. Liu, J. Ding, A. O. Adeyeye, *Europhys. Lett.* **2014**, *108*, 17003.
[37] The TRIM (Transport of Ions in Matter) program, http://srim.org/(accessed January 2016).
[38] J. I. Martín, J. Nogués, K. Liu, J. L. Vicent, I. K. Schuller, *J. Magn. Magn. Mater.* **2003**, *256*, 449.
[39] J. Sort, S. Suriñach, J. S. Muñoz, M. D. Baró, M. Wojcik, E. Jedryka, S. Nadolski, N. Sheludko, J. Nogués, *Phys. Rev. B* **2003**, *68*, 014421.
[40] C. Leighton, H. Suhl, M. J. Pechan, R. Compton, J. Nogués, I. K. Schuller, *J. Appl. Phys.* **2002**, *92*, 1483.
[41] S. Chikazumi, *Physics of Magnetism*, John Wiley & Sons Inc., New York, USA **1964**.
[42] L. Berger, *J. Appl. Phys.* **1978**, *49*, 2156.
[43] K. Hong, N. Giordano, *Phys. Rev. B* **1995**, *51*, 9855.
[44] H.-N. Lin, Y. H. Chiou, B.-M. Chen, H.-P. D. Shieh, C.-R. Chang, *J. Appl. Phys.* **1998**, *83*, 4997.
[45] Y. C. Chang, C. C. Chang, W. Z. Hsieh, H. M. Lee, J. C. Wu, *IEEE Trans. Magn.* **2005**, *41*, 959.
[46] A. Kharmouche, S.-M. Chérif, A. Bourzami, A. Layadi, G. Schmerber, *J. Phys. D: Appl. Phys.* **2004**, *37*, 2583.
[47] M. Löhndorf, A. Wadas, H. A. M. van den Berg, R. Wiesendanger, *Appl. Phys. Lett.* **1996**, *68*, 3635.
[48] M. Cartier, S. Auffret, Y. Samson, P. Bayle-Guillemaud, B. Dieny, *J. Magn. Magn. Mater.* **2001**, *223*, 63.
[49] D. Buntinx, S. Brems, A. Volodin, K. Temst, C. Van Haesendonck, *Phys. Rev. Lett.* **2005**, *94*, 017204.
[50] S. N. Gordeev, J. M. L. Beaujour, G. J. Bowden, B. D. Rainford, P. A. J. de Groot, R. C. C. Ward, M. R. Wells, A. G. M. Jansen, *Phys. Rev. Lett.* **2001**, *87*, 186808.
[51] S. Vandezande, C. Van Haesendonck, K. Temst, *Appl. Phys. Lett.* **2009**, *94*, 192501.
[52] J. Swerts, K. Temst, M. J. Van Bael, C. Van Haesendonck, Y. Bruynseraede, *Appl. Phys. Lett.* **2003**, *82*, 1239.
[53] P. M. Levy, S. Zhang, *Phys. Rev. Lett.* **1997**, *79*, 5110.
[54] A. D. Kent, J. Yu, U. Rudiger, S. S. P. Parkin, *J. Phys.: Condens. Matter* **2001**, *13*, R461.
[55] J. Nogués, I. K. Schuller, *J. Magn. Magn. Mater.* **1999**, *192*, 203.
[56] J. Nogués, J. Sort, V. Langlais, V. Skumryev, S. Suriñach, J. S. Muñoz, M. D. Baró, *Phys. Rep.* **2005**, *422*, 65.
[57] I. K. Schuller, R. Morales, X. Batlle, U. Nowak, G. Güntherodt, *J. Magn. Magn. Mater.* **2016**, *416*, 2.
[58] F. Radu, V. Leiner, K. Westerholt, H. Zabel, J. McCord, A. Vorobiev, J. Major, D. Jullien, H. Humblot, F. Tasset, *J. Phys.: Condens. Matter* **2005**, *17*, 1711.
[59] T. Saerbeck, N. Loh, D. Lott, B. P. Toperverg, A. M. Mulders, M. Ali, B. J. Hickey, A. P. J. Stampfl, F. Klose, R. L. Stamps, *Phys. Rev. B* **2012**, *85*, 014411.
[60] E. Kentzinger, U. Rücker, B. Toperverg, F. Ott, T. Brückel, *Phys. Rev. B* **2008**, *77*, 104435.
[61] B. Toperverg, O. Nikonov, V. Lauter-Pasyuk, H. J. Lauter, *Physica B* **2001**, *297*, 169.
[62] A. Paul, T. Krist, A. Teichert, R. Steitz, *Physica B* **2011**, *406*, 1598.
[63] G. P. Felcher, S. Adenwalla, V. O. de Haan, A. A. van Well, *Nature* **1995**, *377*, 409.
[64] R. W. E. van de Kruijs, H. Fredrikze, M. Th. Rekveldt, A. A. van Well, Yu. V. Nikitenko, V. G. Syromyatnikov, *Physica B* **2000**, *283*, 189.
[65] B. B. Maranville, B. J. Kirby, A. J. Grutter, P. A. Kienzle, C. F. Majkrzak, Y. Liu, C. L. Dennis, *J. Appl. Cryst.* **2016**, *49*, 1121.
[66] S. Brems, D. Buntinx, K. Temst, C. Van Haesendonck, F. Radu, H. Zabel, *Phys. Rev. Lett.* **2005**, *95*, 157202.
[67] G. P. Felcher, R. O. Hilleke, R. K. Crawford, J. Haumann, R. Kleb, G. Ostrowski, *Rev. Sci. Instrum.* **1987**, *58*, 609.
[68] J. Demeter, A. Teichert, K. Kiefer, D. Wallacher, H. Ryll, E. Menéndez, D. Paramanik, R. Steitz, C. Van Haesendonck, A. Vantomme, K. Temst, *Rev. Sci. Instrum.* **2011**, *82*, 033902.
[69] A. R. Wildes, *Rev. Sci. Instrum.* **1999**, *70*, 4241.
[70] E. Babcock, A. Ioffe, *J. Phys.: Conf. Ser.* **2011**, *294*, 012005.

Received: October 15, 2016
Revised: November 11, 2016
Published online: January 9, 2017